Defect Criticality Analysis on Fatigue Life of L-PBF 17-4 PH Stainless Steel via Machine Learning

Anyi Li[a], Shaharyar Baig[b,c], Jia Liu[a,b,] *, Shuai Shao[b,c], Nima Shamsaei[b,c]
[a] Department of Industrial and Systems Engineering, Auburn University, Auburn, AL 36830, USA
[b] National Center for Additive Manufacturing Excellence (NCAME), Auburn University, Auburn, AL 36830, USA
[c] Department of Mechanical Engineering, Auburn University, Auburn, AL 36830, USA

Highlights

- Extract critical defect features from fractography of L-PBF parts by computer vision
- Develop a machine learning framework to correlate defect features and fatigue life
- Generate interpretable insights about defect-fatigue life correlations in L-PBF

Abstract

Defects innate in additively manufactured components may lead to inferior and more scatter in fatigue lives, thus challenging the qualification of these components in fatigue-critical applications. This work seeks to correlate geometrical features of critical defects measured from fracture surfaces to the fatigue performance of laser beam powder bed fusion (L-PBF) components with machine learning and to develop an integrated data-driven analytical framework for defect criticality (IDADC). IDADC has the potential to enhance the understanding of defect-fatigue relationships in a data-driven fashion. The results show that the obtained relationships between the extracted size-related and morphology-related defect features and the fatigue life of L-PBF specimens align with the known fatigue mechanisms and influencing factors. Furthermore, the proposed IDADC framework can model the relationships between defect features and fatigue life with a low mean absolute percentage error of 0.101 using a kernel support vector regression (SVR). This work could establish the algorithmic foundation for nondestructive fatigue evaluation of additive manufacturing products from various facets of critical defects in the future.

Keywords: Additive manufacturing; Laser beam powder bed fusion; Defect criticality; Computer vision; Machine learning

Abbreviations (in the order of appearance):

Acronym	Name
AM	Additive manufacturing
L-PBF	Laser beam powder bed fusion
LOFs	Lack of fusions
CT	Computed tomography
ML	Machine learning
IDADC	Integrated data-driven analytical framework for defect criticality
SEM	Scanning electron microscopy
Sa	Strain amplitude
YS	Yield strength
UTS	Ultimate tensile strength
CBIR	Content-based image retrieval
PCC	Pearson correlation coefficient
MIC	Maximal information coefficient
SSE	Sum of square error
MSE	Mean square error
MAPE	Mean absolute percentage error
RMSE	Root mean square error
NSL	Normalized stress level
DTS	The distance to the surface
ED	Equivalent diameter
MaxFD	Max Feret diameter
MinFD	Min Feret diameter
MajorAL	Major axis length
MinorAL	Minor axis length
SVR	Kernel support vector regression
LASSO	Least absolute shrinkage and selection operator
PFI	Permutation feature importance
ALE	Accumulated local effects

1. Introduction

Additive manufacturing (AM), which creates intricate geometrical 3D objects using layer-wise strategy directly from digital solid models, has transformed from rapid prototyping to a revolutionary digital manufacturing technology for functional and structural applications [1-5]. With its superiority in design flexibility, product customization, and low-volume timely production, AM constitutes a viable alternative to traditional methods of manufacturing [3, 4, 6, 7]. As a metal AM process, laser powder bed fusion (L-PBF) melts metallic powders with a heat source in a layer-wise manner during fabrication and enables nearly limitless flexibility in manufacturing. It dominates the current metal AM market with 86.5% of globally installed AM units being L-PBF [8].

One of the key challenges in adopting AM technologies for functional and structural applications lies in the uncertainty of their fatigue performance [9]. Degraded fatigue strength and a pronounced scatter in the fatigue life of L-PBF components can be attributed to the abundance and variability of L-PBF process-induced defects [10]. In L-PBF, process characteristics, such as a highly dynamic melt pool, ultra-high solidification/cooling rates, and a large thermal gradient, inevitably affect the microstructural traits and result in varying levels of process-induced defects, including entrapped gas-entrapped pores, lack of fusions (LOFs), and keyholes [11]. These defects are one of the major life-limiting factors under cyclic loadings and the dominant mechanisms for fatigue crack initiation in L-PBF components. Fatigue performance of L-PBF components, specifically after surface treatments ridding any significant surface roughness, is potentially influenced by the presence of defects that act as a source of stress concentrations [12, 13]. Locations with a large population of more severe defects such as the LOFs defects may initiate fatigue cracks earlier due to high-stress concentrations in those regions.

Research on the impact of defects on the fatigue performance of L-PBF specimens has gained great traction [14-22]. Defect features, such as type, size, aspect ratio, and distance to the surface, are extracted from fractography and X-ray computed tomography (CT) images, and incorporated into existing fatigue theories (e.g., fracture mechanics-based fatigue life prediction) for analysis. With the advancement of measurements and data analytics, there is a burgeoning need to leverage computer vision and machine learning (ML) [23] to extract defect features and evaluate the critical roles of defects in the fatigue performance of L-PBF specimens.

This study attempts to advance the understanding of defect criticality on fatigue performance by incorporating computer vision and ML in an integrated data-driven analytical framework for defect criticality (IDADC). The rest of the paper is structured as follows: Background information on defect characterization and defect sensitive fatigue modeling are presented in Section 2; the proposed IDADC is detailed in Section 3 with the integration of computer vision, ML, and model-agnostic interpretation for analyzing defect features and understanding defect-fatigue relationships; the experiments and datasets for fatigue tests and microscopy are introduced in Section 4; IDADC is further corroborated with the case studies in Section 5; finally, conclusions and future work are presented in Section 6.

2. Background

This section provides background information on (1) the available AM defect characterization and analysis studies and (2) the common practices in modeling fatigue performance of AM specimens. Based on this review, research gaps are identified for this study.

2.1. Defect characterization and analysis in AM studies

Both destructive and nondestructive inspections can be used to characterize defects in the AM fabricated specimens. Destructive defect inspections typically consist of fractography analysis conducted using microscopy on failed fatigue specimens to determine the defects responsible for the crack initiation and failure of the specimen. Nondestructive defect inspections such as X-ray CT techniques can acquire 3D descriptions of defects within the scanned regions. Currently, defect types (e.g., LOFs, gas-entrapped pores, or keyholes) and a few conventional defect characteristics (e.g., size/area, circularity/sphericity, aspect ratio, and distance to the surface) from the fractography and X-ray CT have been evaluated to understand their impacts on the fatigue performance of metal AM components [14-18]. For example, studies using X-ray CT to examine defects on L-PBF fabricated specimens and investigate the effects of defects on mechanical properties were reviewed in [14]. It showed that fatigue properties are more critical to total porosity extent and proximity of defects to the surface, and the use of X-ray CT and the advances in the quality of L-PBF materials has led to the identification of near-surface pores as critical for fatigue applications.

These studies specifically obtain the defect features, such as size, shape, distance to the surface, from 2D microscopy or 3D X-ray CT images to investigate their relationships with fatigue performance. For instance, Tang and Pistorius [15] examined defects measured on 2D sections of L-PBF AlSi10Mg parts by scanning electron microscope (SEM) and estimated the distribution of defect size by extreme-value statistics. The defect size distribution was used to infer the size of the feasible largest defect and establish the relationships between the size of the largest defect and the fatigue life for prediction. Sanaei et al. [16] studied defects of L-PBF Ti-6Al-4V and 17-4 PH stainless steel (SS) specimens and the relationships between the defect characteristics (e.g., size, sphericity/circularity, aspect ratio) and fatigue life. Based on the defect description with both 2D microscope and 3D X-ray CT, it was noted that the aspect ratio and circularity/sphericity of the defects typically decreased as the defect size increased; the largest defects had low circularity/sphericity and aspect ratio and created high stress-concentrations which made them critical to the fatigue performance of specimens. The variability of defect characteristics based on their location in these specimens was also studied.

Tammas-Williams et al. [17] identified critical defects by ranking porosity defects in electron beam-powder bed fusion (EB-PBF) fabricated Ti-6Al-4V specimens according to four defect features: size, aspect ratio, distance to the surface, and distance to other pores from X-ray CT scans. According to authors-defined ranking rules, the defects with high ranks (i.e., large pore size, small aspect ratio, small distance to the surface, and/or small distance to other pores) were considered detrimental to fatigue life. The experiments verified that the actual crack-initiating defects were among the top 3% defects in their rankings. Maskery et al. [18] used X-ray CT to quantify and characterize defects in L-PBF AlSi10Mg parts in terms of size, aspect ratio, and circularity. The data showed that the largest defects in the L-PBF material were strongly anisotropic, flat, and disc-like parallel to the layers of the manufacturing process. Moreover, the defect size, aspect ratio, and circularity were unaffected by the heat treatments, despite the changes in microstructure and hardness.

The abundance and variability of L-PBF process-induced defects can cause degraded fatigue strength and a pronounced scatter in the fatigue life of the fabricated components [10]. Moreover, a systematic investigation and analysis of the defects on fatigue performance remain unexplored, and therefore, defect features (such as morphological features) have not yet been widely used in conventional fracture-mechanics-based fatigue modeling for L-PBF parts.

2.2. Fatigue behavior modeling of metallic materials

The fatigue modeling of metallic materials can be classified into three main categories, namely: empirical, analytical, and computational methods. Empirical models, such as the ones proposed by Coffin-Manson and Basquin, analyze the material's fatigue parameters from experimental data through curve fitting [24, 25]. These methods are very commonly used due to their simplicity and high accuracy.

However, one of their limitations is that they do not explicitly consider the effect of surface roughness and defects inherent in AM materials; therefore, a new set of data needs to be generated with any change in defects.

As an alternative, analytical methods such as fracture-mechanics-based fatigue models allow the fatigue strength to be evaluated with the assumption that cracks and flaws exist, and the fatigue life is governed by the propagation of these cracks [26]. Fracture-mechanics-based defect-sensitive fatigue models have been applied to correlate limited defect features with the fatigue performance of additively manufactured parts [27-29]. Commonly adopted hypotheses in such fatigue analysis are that defects behave as "short cracks" and that the fatigue limit is inversely related to the crack size [30, 31]. Stern et al. [32] examined the correlation between 3D information of process-induced defects gained by microfocus CT and fatigue behavior. Their results depict that fatigue life is significantly affected by the size and orientation of defects. Therefore, the current popular fatigue performance assessment framework of AM metallic materials includes estimating the size of the largest defects by the statistics of extremes with a Gumbel distribution based on Murakami's $\sqrt{area}$ parameter, relating the defect size to the fatigue limit by El-Haddad's model, and determining the infinite life regime by the Kitagawa-Takahashi diagram. In the finite life regime, one can calculate the fatigue life by assuming the defect as the initial crack and integrating the fatigue crack growth rate from Paris' law and using a crack growth model such as NASGRO [33-36]. Kotzem et al. [37] currently adopt $\sqrt{area}$ parameter model to investigate the dependency of defect size and resulting stress amplitude-number of cycles to failure (S-N) curve based on artificial defects with defined geometry and size. Nevertheless, to accurately predict the fatigue performance of AM materials, it is also important to consider the crack initiation stage as well as the effect of the resultant AM microstructure. Due to the nature of AM processes, where any changes in the process parameters and post-process procedures may result in a unique micro-defect structure, it is not always practical to use empirical or analytical tools.

To this end, physics-based computational models such as crystal plasticity models, with their ability to explicitly model the deformation mechanisms involving defects and constituent phase, are uniquely appealing. In fact, crystal plasticity simulations have been used to model the crack initiation and early growth behaviors in various materials under cyclic loading [38-42]. In these simulations, a fatigue indicator parameter, such as the Fatemi and Socie parameter based on shear strain amplitude and maximum normal stress [43] as well as ones based on cumulative plastic strain or plastic strain energy [42], is typically needed to monitor the evolution of local fatigue damage in the microstructure and crack initiation. However, these computations are limited in length scale, and it is generally challenging for them to assess the stable growth behavior of long fatigue cracks.

Recently, data-driven approaches have been promising in understanding the relationships between various AM parameters on the structure and fatigue behavior of AM materials [44]. The proliferation of AM technologies has allowed large databases of AM mechanical data to be generated. Such databases can be used in data-driven models such as ML to identify trends and relationships amongst various AM parameters, micro-/defect-structure and part performance. To utilize the increasingly abundant data on defects in L-PBF parts with the advancement of sensing and microscopy, this study attempts to advance the conventional practice in understanding the defect criticality on fatigue performance by adopting computer vision and ML for defect feature extraction and analysis. The proposed IDADC can efficiently explore a large amount of data, extract multi-facet data features, and discover subtle feature patterns to substantially improve the understandings of defect-fatigue relationships. Moreover, it can pave the way for data-driven prediction for fatigue life with physical-based interpretation by integrating domain knowledge and model-agnostic methods.

3. Methodology

In this study, an IDADC is developed to explore and understand the relationships between various defect features captured from fractography images and the fatigue life of L-PBF specimens. The fractography images are captured by SEM on the fracture surface of failed fatigue specimens to determine the defect responsible for the crack initiation and failure of the specimens. Only those defects which were identified as being responsible for initiating fatigue cracks were considered in the IDADC. The IDADC consists of three primary elements as follows and is summarized in Figure 1:

1) Defect feature extraction: content-based image retrieval (CBIR) [45], a computer vision technique, describes defect characteristics on fractography images with various numerical descriptors.
2) Correlation analysis: Pearson correlation coefficient (PCC) and maximal information coefficient (MIC) are integrated to analyze the linear and nonlinear relationships between the defect features and fatigue life of L-PBF specimens.
3) Defect-fatigue modeling: a novel machine learning model, kernel support vector regression (SVR) with model-agnostic interpretation, is developed to identify the critical defect features and quantify their marginal impacts on the fatigue life of the L-PBF specimens.

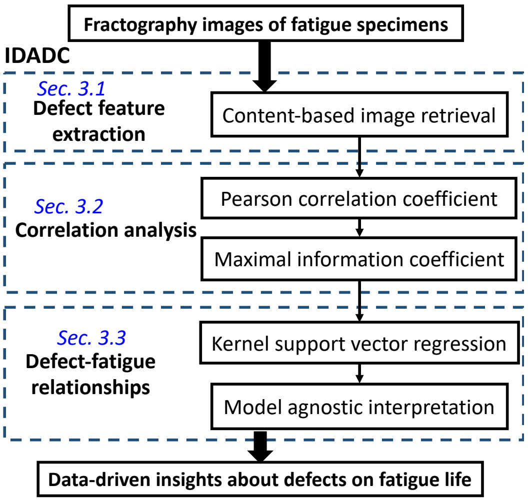

Figure 1. The proposed IDADC for understanding defect-fatigue relationships in L-PBF specimens via data-driven analytics.

This IDADC provides a novel data-driven perspective to investigate the effect of defects on fatigue performance and identify the critical defects that may initiate cracks in the specimen under fatigue loading. It can bridge the current research gaps by examining the defect characteristics systematically and their relationships with the fatigue life of L-PBF specimens. The outcomes and insights from the framework can be used to enhance the understandings from experimental studies and improve fatigue life evaluation for L-PBF materials.

3.1. Defect feature extraction

For crack-initiating defects (referred to as just defects from hereon) in L-PBF specimens on the 2D fractography images, as shown in Figure 2 (a), a variety of defect features can be extracted from the defect contours (some of which are shown in Figure 2 (b)) by CBIR to characterize distinctive aspects of defects. In addition to the conventional features, like area, perimeter, circularity, aspect ratio, other "unconventional" features can also shed light on various defect characteristics. They include: eccentricity, which is the ratio of the distance between the foci of the outer ellipse and its circularity, describes how close the defects are to a circle; solidity, which is the ratio of a defect area filling its convex hull, indicates whether the defects are convex and compact with an irregular shape; and angularity, which calculates the error of a defect contour to fit an ellipse, implies the smoothness of defect boundary and the potential existence of sharp angles. Some of the extracted features are depicted in Figure 2 (c).

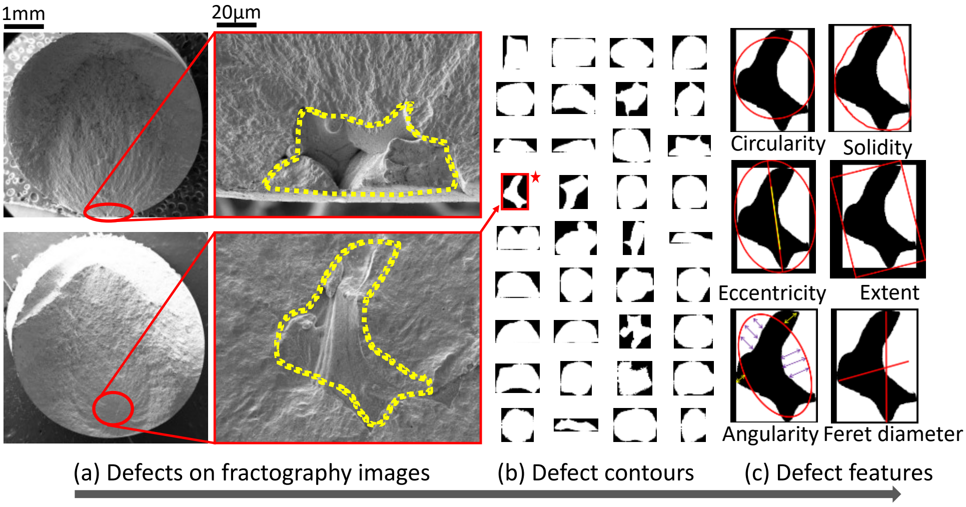

Figure 2. The procedure and illustrations of defect feature extraction from fractography images using CBIR techniques.

All the extracted defect features, including by CBIR, are summarized in Table 1 with their respective definitions. They can be categorized into size-related, morphology-related, and distance-related features. Moreover, fatigue life is also influenced by subsequent post-processing thermal heat treatments [46, 47] and stress response levels in the fatigue tests. Thus, strain amplitude and normalized stress level parameter derived from the stress response and ultimate tensile strength are also included in the analysis as process-related features. All these features are utilized to quantify various aspects of defects and to investigate the relationships between defects and fatigue life of L-PBF specimens, as they are affected by the level of ductility induced by the post-fabrication heat treatment in this study.

Table 1 Defect features from fractography images and process-related features of L-PBF specimens.

Category	Descriptors (Features)	Definition
Size	Major axis length	a
	Minor axis length	b
	Area	S
	Convex area	S_C
	Bounding box area	$S_B = a \times b$
	Equivalent diameter	D_E
	Perimeter	C
	Max Feret diameter	D_f^{Max}
	Min Feret diameter	D_f^{Min}
Morphology	Eccentricity	$Eccentricity = \frac{Distance\ between\ the\ foci\ of\ the\ outer\ ellipse}{a}$
	Circularity	$Circularity = \frac{4\pi \times S}{S_C^2}$
	Solidity	$Solidity = \frac{S}{S_C}$
	Extent	$Extent = \frac{S}{S_B}$
	Angularity	$Error\ of\ a\ shape\ to\ fit\ an\ ellipse$
Distance	Distance to the surface	$Distance\ to\ the\ specimen\ external\ surface$
Process	Strain amplitude	S_a
	Ultimate tensile strength	UTS
	Normalized stress level	$\frac{S_a}{UTS}$

3.2. Correlation analysis

In the proposed IDADC, Pearson correlation coefficient (PCC) [48] and maximal information coefficient (MIC) [49] are adapted for correlation analysis to explore and quantify the linear/nonlinear relationships between the fatigue life of L-PBF specimens and various defect features and the interdependence among those defect features. PCC is a widely used statistic to measure the linear correlation between two variables *X* and *Y*.

$$r(X,Y) = \frac{\sum_{i=1}^{n}(x_i - \bar{x})\,(y_i - \bar{y})}{\sqrt{\sum_{i=1}^{n}(x_i - \bar{x})^2}\,\sqrt{\sum_{i=1}^{n}(y_i - \bar{y})^2}} \tag{1}$$

where $\{(x_i, y_i), i = 1, \dots, n\}$ are the observed data points for the two variables, n is the number of data points in the dataset. PCC takes values between -1 and 1, with 0 means statistical independence between two variables *X* and *Y*, -1 means a completely negative relationship, and 1 means a completely positive relationship.

Moreover, MIC is an information-theory-based measure of association that can capture a wide range of linear or nonlinear relationships between variables. MIC is formulated based on a naive mutual information estimate $I_{MIC}\{x, y\}$ via a data-dependent binning scheme:

$$MIC(x,y) = \max \frac{I_{MIC}\{x,y\}}{\log_2 \min\{n_X, n_Y\}} \tag{2}$$

$$I_{MIC}\{x,y\} = \sum_{\tilde{x},\tilde{y}} \hat{p}(\tilde{x},\tilde{y}) \log_2 \frac{\hat{p}(\tilde{x},\tilde{y})}{\hat{p}(\tilde{x})\,\hat{p}(\tilde{y})} \tag{3}$$

where n_X, n_Y denote the number of bins imposed on the x, y axes; $\hat{p}(\tilde{x},\tilde{y})$ is the fraction of data points falling into the bin $(\tilde{x},\tilde{y})$. The MIC binning scheme is chosen to maximize the ratio in Eq. (2) with the total number of bins $(n_X \times n_Y)$ in the user-specified threshold. MIC takes values between 0 and 1, with 0 means statistical independence between two variables *X* and *Y*, and 1 means a completely noiseless dependence. However, MIC is computationally expensive and does not indicate the direction or the sign of the relationships.

Correlation analysis is a straightforward and intuitive data-driven step to understand the relationships between defect features and fatigue life. The results from correlation analysis can highlight the critical defect features and the strength/direction they impact the fatigue life.

3.3. Defect-fatigue relationships

The correlation analysis in Section 3.2 explores the relationships between the fatigue life of L-PBF specimens and individual defect features. The IDADC then utilizes the kernel support vector regression (SVR) to understand how defect features concurrently impact fatigue life by establishing a surrogate model with model-agnostic interpretation.

3.3.1. Kernel support vector regression

In IDADC, SVR [50] aims to formulate a nonlinear surrogate model with a kernel function to model the fatigue life of an L-PBF specimen from various defect features. It can map the nonlinear relationships between defect features and fatigue life into a high-dimensional space (which can be linearly segmented) via the kernel function and approximate the fatigue life with linear relationships in this high-dimensional space.

With the defect features of L-PBF specimens extracted by CBIR in Section 3.1 and the experimentally obtained fatigue life values, we denote the dataset as $D_i = (\boldsymbol{x}_i, y_i), i = 1,2,3, \dots, n$, where $\boldsymbol{x}_i = (x_{i1}, x_{i2}, \dots, x_{id})^T$ are d defect features of the specimen i, and y_i denotes the fatigue life of the specimen i. Radial basis kernel $K(\boldsymbol{x}_i, \boldsymbol{x}_j) := \langle \Phi(\boldsymbol{x}_i), \Phi(\boldsymbol{x}_j) \rangle = e^{-\gamma \|x_i - x_j\|^2}$ has strong ability to fit nonlinear and high-dimensional defects data sets and it overcomes the space complexity problem as it just need to store the support vectors. Therefore, a nonlinear mapping function $\Phi(\boldsymbol{x}_i)$ is implicitly represented by a radial basis kernel used for all data sets in this SVR, with $\gamma > 0$ (it controls the curvature of decision boundary) selected by grid search. The SVR model can be simply written in a matrix format

$$f(\Phi(\boldsymbol{X})) = \Phi(\boldsymbol{X})\boldsymbol{w} + b \tag{4}$$

where $\boldsymbol{X} = (\boldsymbol{x}_1, \boldsymbol{x}_2, \dots, \boldsymbol{x}_n)^T$ is the matrix for defect features in the training data, $\boldsymbol{w} = (w_1, w_2, \dots, w_d)^T$ are the regression coefficients, and b is the bias in regression. To solve this SVR problem, its objective function can be formalized as follows

$$\begin{aligned} &\min_{\boldsymbol{w},\boldsymbol{b}} \frac{1}{2}\|\boldsymbol{w}\|^2 + C\sum_{i=1}^{n}(\xi_i + \hat{\xi}_i) \\ &s.t.\ \ \Phi(\boldsymbol{x}_i)\boldsymbol{w}^T + b - y_i \le \epsilon + \xi_i, \\ &\qquad y_i - \Phi(\boldsymbol{x}_i)\boldsymbol{w}^T - b \le \epsilon + \hat{\xi}_i, \\ &\qquad \xi_i > 0, \hat{\xi}_i > 0, i = 1,2,\dots,n \end{aligned} \tag{5}$$

where $\|\boldsymbol{w}\|^2$ is the magnitude of the normal vector to the surface that is being approximated, C denotes regularization constant, ξ_i and $\hat{\xi}_i$ are slack variables to guard against outliers, and ϵ is the soft margin in SVR. This model can be solved by the Lagrange multiplier method with satisfying Karush–Kuhn–Tucker (KKT) conditions [51, 52]. Consequently, with the SVR in Eq. (4), the relationships between defect features and fatigue life of L-PBF specimens can be modeled in a data-driven fashion.

3.3.2. Interpretation with model-agnostic methods

In IDADC, model-agnostic interpretation methods are integrated to explain the importance of defect features to the response of fatigue life in “black-box” SVR via a variety of graphics generated based on importance analysis [53]. Permutation feature importance (PFI) and accumulated local effects (ALE) are used in this study. PFI measures the importance of a feature by calculating the increase in the model error after permuting the feature. A feature is “important” if shuffling its values increases the model error. Mean absolute error (MAE) is selected as the error function in this study.

ALE describes the dependence of features on ML outcomes, even when the features are correlated. It demonstrates the marginal effect of interested features (in set S) on the ML outcomes by marginalizing the ML model output over the distribution of the other features in set C. Therefore, the function shows the relationships between the interested features and the model outcomes. It is realized by averaging the changes in the model outcomes and accumulating them over the grid. To estimate local effects, we divide the feature into many intervals and compute the differences in the model outcomes.

$$\hat{f}'_{s,ALE}(x) = \sum_{k=1}^{k_s(x)} \frac{1}{n_s(k)} \sum_{i: x_s^{(i)} \in n_s(k)} f\left(z_{k,s}, \boldsymbol{x}_c^{(i)}\right) - f\left(z_{k-1,s}, \boldsymbol{x}_c^{(i)}\right) \tag{6}$$

where $\hat{f}$ is the ML surrogate model; $\boldsymbol{x}_s$ are the interested features in set S and $\boldsymbol{x}_c$ are the other features in set C; z's is a grid of intervals over which we compute the changes in the outcome of the ML model. This effect is centered so that the mean effect is zero.

$$\hat{f}_{s,ALE}(x) = \hat{f}'_{s,ALE}(x) - \frac{1}{n} \sum_{i=1}^{n} \hat{f}'_{s,ALE}\left(\boldsymbol{x}_s^{(i)}\right) \tag{7}$$

ALE plots are centered at zero, and the value at each point of the ALE curve is the difference to the mean outcomes. Thus, they indicate the relative effect of changing the feature on the model outcomes.

4. Experiments and Data Collection

4.1. Materials, fatigue testing, and fractography

Fracture surface information from L-PBF 17-4 PH SS fatigue test specimens is used for integrated data-driven analysis and modeling in this study. The samples were fabricated as part of three previous studies [19, 54, 55] on an EOS M290 L-PBF AM system under an argon-shielded atmosphere [19]. EOS recommended process parameters for 17-4 PH SS, presented in Table 2, were used to fabricate 11 mm square bars in studies [55, 56] and three different geometries of dog-bone, small block, and large block in study [19]. Subsequently, all the printed samples were surface machined to fatigue specimen geometries following recommendations from ASTM E606, details of which can be found in [19, 54, 55]. Heat-treatment was performed for the different batches of specimens following ASTM

A693 [57] using five conditions of H900, H1025, CA-H900, CA-H1025, and CA-H1150). Fatigue tests were performed in the previous studies according to ASTM E606 under fully-reversed (R = -1), strain-controlled mode under strain amplitudes of 0.0025 mm/mm, 0.003 mm/mm, and 0.004 mm/mm on an MTS servo-hydraulic load frame [19, 54, 55]. The stress response of the material was recorded from the fatigue tests as well as the strain-life data. Tensile tests were also performed as per ASTM E8 to determine some of the parameters used in the analysis, such as the yield strength (YS) and the ultimate tensile strength (UTS). A combination of optical microscopy using a Keyence VHX-6000 capable of imaging up to a 1000x magnification and scanning electron microscopy using a Zeiss Crossbeam 550 SEM capable of imaging up to a 1,000,000x magnification, were performed to acquire the fractography images. The resolution for these two imaging techniques depends on the scan settings, and can be up to 1 μm for optical microscopy and 4 nm for scanning electron microscopy. More details on the fabrication, post-processing, tensile, and fatigue testing conditions can be found in references [19, 54, 55]. The final image data was split into categories based on the testing strain amplitudes and the heat treatments for training/validating the developed IDADC framework.

Table 2 Default L-PBF core process parameters for 17-4 PH SS as provided by EOS and used to fabricate all the specimens in this study.

Laser power (W)	Scanning speed (mm/s)	Hatching distance (μm)	Layer thickness (μm)
220	755.5	100	40

4.2. Data acquisition

One hundred and ninety 2D fractography images of critical defects for L-PBF 17-4 PH SS specimens (in machined surface condition) are captured. Critical defects on the fracture surface are the defects likely to initiate the cracks. If there are multiple defects on the fracture surface and they are far away from each other, we identified one critical defect based on experience and extract its features for the analysis. If defects are connected on the fracture surface, we treated them as one critical defect. There are six main categories based on the different strain amplitudes in the strain-controlled fatigue tests (i.e., 0.001 mm/mm, 0.0015 mm/mm, 0.0020 mm/mm, 0.0025 mm/mm, 0.003 mm/mm, 0.004 mm/mm) with 8, 6, 47, 17, 62, and 50 defects, respectively. It is worth noting that the dataset for the L-PBF specimens under different strain-controlled fatigue tests and heat treatments used in this study is limited for the proposed ML methods. In general, the model accuracy of ML relies on both the data size and the data quality (e.g., the consistent conditions under which the datasets are collected) [23]. Therefore, we selected three disparate datasets for analysis and investigation in this study by making tradeoffs between the data size and consistency in conditions (i.e., strain-controlled fatigue tests and heat treatments). Any outliers were removed from the selected datasets based on the key values of fatigue life, defect size, and the distance proximity to the surface shown in Figure 3. The thresholds for separating outliers from all data are 330,984 cycles, 143,400 μm^2 and 6.3 μm for fatigue life, defect size, and the distance proximity to the surface, respectively.

(1) Dataset 1 (large data size, but low consistency): 157 defects on all L-PBF 17-4 PH SS fatigue testing specimens.

(2) Dataset 2 (medium data size, and medium consistency): 51 defects on L-PBF 17-4 PH SS specimens with different heat treatments in fatigue tests at a strain amplitude of 0.003 mm/mm.

(3) Dataset 3 (small data size, but high consistency): 34 defects on L-PBF 17-4 PH SS specimens with heat treatment of CA-H1025 and fatigue tests at a strain amplitude of 0.003 mm/mm.

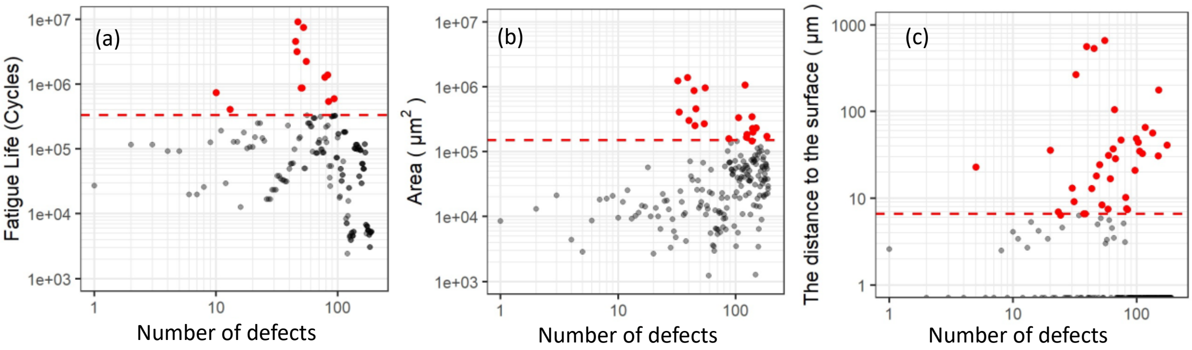

Figure 3. The selection of outliers for all data. (a) Outliers of fatigue life of L-PBF specimen; (b) Outliers of area of L-PBF specimen; and (c) Outliers of the distance to the surface of L-PBF specimen. Note: Red points mean outliers, red dash line is the threshold between outliers and normal points and all data are displayed in a logarithmic coordinate system)

The experimental datasets used for understanding the relationships between defect features and fatigue life are shown in Table 3. In addition, we will investigate whether data size or consistency in conditions is important in understanding the relationships in the proposed IDADC framework.

Table 3 Datasets used in the IDADC for understanding defect-fatigue relationships.

	Strain level (mm/mm)	Heat treatment	Total data points	Outliers removed	Remaining data points
Dataset 1	All	All	190	33	**157**
Dataset 2	0.003	All	62	11	**51**

Dataset 3	0.003	CA-H1025	43	9	**34**

5. Case Study

5.1. Feature extraction

Defect feature extraction from the 2D fractography images is implemented via CBIR on the three datasets in this study. As shown in Table 1, the extracted defect features describe various aspects of defect characteristics. These defect features can be summarized statistically to provide an overview of the defects. For instance, the statistics of defect features extracted from Dataset 3 (strain level of 0.003 mm/mm and heat treatment of CA-H1025) are summarized in Table 4. It is noticeable from Table 4 that:

(1) The distributions of size-related features are skewed to the right, and most defects have smaller values than their means. It indicates that exceedingly large defects are uncommon in the specimens.

(2) The morphology-related features are within the range [0, 1], and are not as skewed as size-related features. These numbers describe whether the defects are close to an ellipse or a circle (eccentricity, circularity), whether they have a regular and smooth boundary or sharp angles (solidity, angularity), whether they are convex and compact (solidity, extent).

(3) Around half of the defects are open on the surface (with distance to the surface as 0 μm).

(4) The distributions of the fatigue lives of these specimens are also skewed to the right, with the majority of specimens having shorter fatigue lives than their mean. The longest fatigue life is around six times the mean and ten times the median. It indicates that some scatter exists in the fatigue life data at the strain amplitude of 0.003 mm/mm.

Table 4 Statistics summary of CBIR-extracted defect features for Dataset 3 (strain level of 0.003 mm/mm and heat treatment of CA-H1025).

Category	Defect features	Mean	Std.	Min.	Median	Max.
Size	Area (μm^2)	3320.2	9271.2	41.1	450.5	46215.8
	Convex area (μm^2)	3334.5	9501.7	43.2	432.6	49642.5
	Major axis length (μm)	53.1	58.6	7.7	30.3	275.8
	Minor axis length (μm)	32.9	41.4	6.7	19.2	209.8
	Equivalent diameter (μm)	40.0	47.0	6.9	22.7	230.1
	Perimeter (μm)	179.4	217.3	29.9	98.1	1115.2
	Max Feret diameter (μm)	55.7	62.9	8.4	30.9	304.1

	Min Feret diameter (μm)	33.6	42.1	7.3	18.5	216.4
Morphology	Eccentricity	0.7	0.2	0.2	0.7	1.0
	Circularity	0.5	0.1	0.3	0.6	0.8
	Solidity	0.9	0.0	0.8	1.0	1.0
	Extent	0.7	0.1	0.4	0.8	0.8
	Angularity	0.2	0.1	0.0	0.2	0.4
Distance	The distance to the surface (μm)	27.3	93.0	0.0	0.0	562.4
	Fatigue life (Cycles)	209015	270613	26735.0	126971.0	1395858.0

These defect features constitute the explanatory variables in the dataset for discovering the relationships between defect features and fatigue life of specimens, while the fatigue life of these L-PBF 17-4 PH SS specimens is the target variable in the following analysis and modeling. Furthermore, since fatigue life is also affected by subsequent post-processing thermal heat treatments [46, 47] and strain amplitude in the fatigue tests, a normalized stress level parameter (derived from UTS and the stress level to adjust the effect of heat treatment) and the strain amplitude are also included as explanatory variables in further analysis.

5.2. Correlation analysis

5.2.1. Correlations between defect features and fatigue life

Correlation analysis between various defect features and fatigue life are implemented with PCC and MIC for three fatigue testing datasets in Table 5. PCC captures positive/negative linear correlations between fatigue life and respective defect features, while MIC indicates the magnitudes (without signs) of (linear and nonlinear) correlations between fatigue life and respective defect features, as shown in Table 5.

Table 5 PCC and MIC between fatigue life of L-PBF 17-4 PH SS specimens and all the defect features for three datasets in this study. The bold values indicate relatively high correlations (≥0.5).

	Dataset 1		Dataset 2		Dataset 3	
Defect Features	PCC	MIC	PCC	MIC	PCC	MIC
strain amplitude	**0.57 (-)**	**0.85**	N/A	N/A	N/A	N/A
Normalized stress level	**0.53(-)**	**0.84**	0.11(-)	0.47	N/A	N/A
Major Axis Length	0.24 (-)	**0.54**	**0.59 (-)**	**0.69**	**0.57 (-)**	**0.72**
Circularity	0.22 (+)	**0.56**	**0.62 (+)**	**0.64**	**0.52 (+)**	0.46
Max Feret Diameter	0.22 (-)	**0.57**	**0.60 (-)**	**0.60**	**0.58 (-)**	**0.62**
Eccentricity	0.21 (-)	**0.54**	**0.52 (-)**	**0.74**	0.43 (-)	**0.56**
Perimeter	0.21 (-)	0.49	**0.61 (-)**	**0.59**	**0.58 (-)**	**0.53**
Solidity	0.18 (+)	0.41	0.49 (+)	**0.54**	0.25 (+)	0.37
Extent	0.18 (+)	**0.61**	**0.54 (+)**	**0.51**	0.38 (+)	**0.56**
Minor Axis Length	0.15 (+)	0.33	0.07 (-)	0.37	0.35 (-)	0.40
Min Feret Diameter	0.13 (+)	0.34	0.41 (-)	0.37	0.39 (-)	0.34

Distance to the surface	0.13 (+)	0.36	0.21 (+)	0.45	0.18 (+)	0.43
Equivalent Diameter	0.12 (-)	0.42	**0.54 (-)**	0.46	**0.52 (-)**	0.41
Convex Area	0.08 (-)	0.44	**0.55 (-)**	**0.54**	**0.51 (-)**	0.49
Area	0.08 (-)	0.42	**0.53 (-)**	0.46	**0.50 (-)**	0.41
Filled Area	0.08 (-)	0.42	**0.53 (-)**	0.46	**0.50 (-)**	0.41
Angularity	0.05 (+)	0.42	0.07 (-)	0.44	0.07 (-)	0.39

* Sorted by descending order of PCC in Dataset 1

Some insights can be inferred from the results in Table 5 for the three datasets:

(1) Dataset 1:

   a. Strain amplitude in strain-controlled fatigue tests and normalized stress level (adjusted by the heat treatment) of materials have much larger PCC and MIC values than the defect features.

   b. The defect features manifest relatively small PCC with fatigue life; however, their impacts on the fatigue life align with known fatigue mechanisms and influencing factors, e.g., defects with larger values in size-related features lead to shorter fatigue life, specimens with circular and less elongated defects tend to have longer fatigue lives, and defects with a smaller value of the distance to the surface lead to shorter fatigue life.

(2) Dataset 2:

   a. Since these specimens are in the same strain-controlled fatigue tests (strain level of 0.003 mm/mm), the defect features are not dominated by the testing conditions but exhibit strong relationships with fatigue life. In addition, they have the same positive/negative impacts on fatigue life as in Dataset 1.

   b. Both PCC and MIC identify similar defect features having strong relationships with the fatigue life of L-PBF17-4 PH SS specimens. They are the size-related features (perimeter, max Feret diameter, major axis length, equivalent diameter, convex area, area, filled area) and morphology-related features (circularity, aspect ratio, extent). The distance to the surface also shows a positive correlation, i.e., defects with a smaller value of the distance to the surface lead to shorter fatigue life.

(3) Dataset 3:

a. All specimens underwent the same heat treatment, CA-H1025, and were tested at the same strain amplitude, i.e., 0.003 mm/mm; this dataset could provide the most accurate results due to the consistent conditions in the test specimens.
b. Despite a small number of test specimens, the PCC and MIC identify similar size-related and morphology-related defect features as in Dataset 2, which have strong relationships with the fatigue life of L-PBF specimens.
c. The distance to the surface also shows a similar positive correlation as in Dataset 2, i.e., defects with a smaller value of the distance to the surface lead to shorter fatigue life.

Despite the differences in these three datasets, both PCC and MIC identify some shared size-related and morphology-related defects features with high correlation values with the fatigue lives of the L-PBF 17-5 PH SS specimens, bolded in Table 5. For instance, these defect features have high PCC and MIC values in all three datasets: max Feret diameter and major axis length (indicate the size and the elongation of the defects), perimeter (indicates the size of the defects and the smoothness of the defect contours), as well as eccentricity and circularity (indicate the elongation and the roundness of the defects). Therefore, these individual defect features exhibit the relationships with fatigue life, and together they can characterize different types of defects (e.g., gas-entrapped pores, LOFs) and enhance the understandings of their impacts on fatigue life. For instance, compared to LOFs, gas-entrapped pores are usually smaller (with a small perimeter, a small max Feret diameter, and/or a small major axis length) and rounder (with a large circularity and/or a small eccentricity). If gas-entrapped pores are critical defects of an L-PBF specimen, the fatigue life of the specimen tends to be longer than a counterpart L-PBF specimen with LOFs as the critical defects.

5.2.2. Correlations among features in defect analysis

We further explore the correlations among the features and visualize their interdependence in correlation matrices in Figure 4. These features are categorized into the size-related defect features, morphology-related defect features, the distance to the surface, and process features (normalized stress level and strain amplitude).

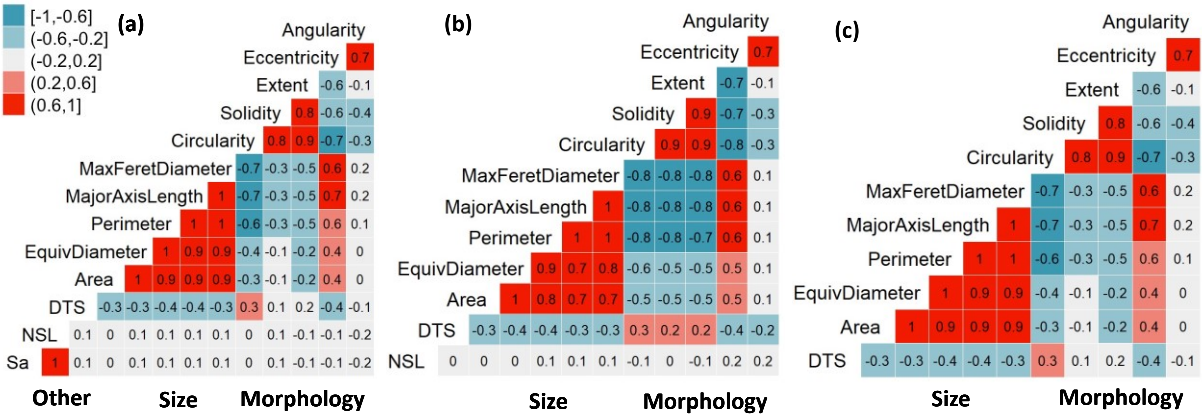

Figure 4. PCC among extracted features of L-PBF 17-4 PH SS specimens: (a) Dataset 1 with all specimens; (b) Dataset 2 with fatigue tests at a strain amplitude of 0.003 mm/mm; and (c) Dataset 3 with heat treatment of CA-H1025 and fatigue tests at a strain amplitude of 0.003 mm/mm. (NSL: Normalized stress level; DTS: The distance to the surface)

Within each category of defect features, the correlations among the respective features are relatively high. For example, the size-related features, e.g., area, perimeter, equivalent diameter, major axis length area, are all highly correlated with each other. Between the categories of defect features, it is noted that a few size-related defect features (i.e., max Feret diameter, major axis length, perimeter) have strong correlations with morphology-related defect features (eccentricity, circularity, solid, extent). In detail, defects with a large max Feret diameter, or major axis length, or perimeter tend to have noncircular shapes (with large eccentricity but small circularity, solidity, and extent). These defects are most likely LOFs; therefore, such correlations can help in the classification of defects and determination of their effects on the fatigue behavior of the materials.

5.3. Defect-fatigue data-driven surrogate modeling

5.3.1. Model accuracy

In the IDADC framework, SVR forms a surrogate model for determining the relationships between defect features and fatigue life for the three datasets. The modeling accuracy is evaluated by mean absolute percentage error (MAPE), a percentage error between the actual fatigue lives and the SVR outcomes, via 5-fold cross-validation.

Three benchmark methods, least absolute shrinkage and selection operator (LASSO), decision tree, and random forests are adopted to compare with SVR in this study. LASSO fits the linear relationships between the target variable (i.e., fatigue life) and explanatory variables (i.e., various defect features) by performing variable selection and regularization simultaneously; decision trees generate rule-based relationships in a tree structure by splitting the dataset on decision nodes according to the values of the explanatory variables; random forests construct a multitude of decision trees and output a mean regression value of the individual trees.

The experiment is based on 5-fold cross-validation to train these machine learning models using data set 1, dataset 2 and dataset 3 to avoid overfitting and improve the generalizability of models shown in Table 6.

Table 6 Comparisons of modeling error of different ML methods via 5-fold cross-validation in predicting fatigue life from defect features in terms of MAPE for testing data for three datasets. Note: the MAPE in the table is composed of average MAPE of 5-fold datasets with its standard deviation.

Dataset	LASSO	Decision trees	Random forest	SVR
Dataset 1	0.891 ± 0.0461	0.948 ± 0.1292	0.800 ± 0.0924	**0.633 ± 0.0477**
Dataset 2	0.541 ± 0.1802	0.454 ± 0.1192	0.385 ± 0.1201	**0.336 ± 0.1049**
Dataset 3	0.651 ± 0.1942	0.575 ± 0.3515	0.578 ± 0.2212	**0.573 ± 0.2037**

It is noted in Table 6 that SVR outperforms the other three benchmark methods with the smallest MAPE and less variance for all three datasets. Decision trees have the largest MAPE values for dataset 1, indicating the rule-based method cannot accurately represent the relationships between the defect features and the fatigue life in different heat treatments and applied strain amplitudes. LASSO also underperforms since the relationships between the defect features and fatigue life are unlikely to be linear. As an ensemble learning method of decision trees, random forests gain modeling accuracy improvement by approximating sophisticated nonlinear relationships, and have relatively small MAPE values, especially for Dataset 2. It indicates that SVR is capable of well predicting fatigue life of L-PBF specimens.

From the data perspective, Dataset 2 and Dataset 3 are generated under consistent conditions (i.e., Dataset 2 includes L-PBF specimens tested under the same strain amplitude, i.e., 0.003 mm/mm, Dataset 3 includes L-PBF specimens that underwent the same heat treatment and tested under the same strain amplitude); therefore, despite the small data sizes, the possible clear patterns in the datasets under the consistent conditions enable accurate modeling of the relationships between defect features and fatigue life. On the contrary, due to the different heat treatment and strain values applied, Dataset 1 with all the specimens has inferior modeling accuracy and is not favorable for analyzing defect criticality despite its relatively large data size.

Table 7 SVR modeling error under different hyperparameters of all datasets via 5-fold cross validation. Note: γ controls the curvature of decision boundary in radial basis kernel; C controls error in the objective function Eq. (5); Bold numbers represent the best MAPE.

Dataset	**Hyperparameters of SVR**		**Error Measurement**
	γ (> 0)	C	MAPE
Dataset 1	0.5	4	0.224
Dataset 2	0.5	4	**0.101**
Dataset 3	0.5	4	0.120

Then we select the best SVR hyperparameters from 5-fold cross-validation grid search to train all datasets and obtain the best prediction error shown in Table 7. These SVR results are used to be interpreted to explore the impact of defects features on the predicted fatigue life by model-agnostic methods in next section.

5.3.2. Model interpretability and result discussion

In the IDADC, we leverage the model-agnostic methods (PFI and ALE) to enhance the result interpretations for SVR. Specifically, we firstly adopt PFI to evaluate the marginal importance of defect features towards the SVR outcomes of fatigue life. Then, we use ALE to further examine how important defect features influence the expected outcomes of SVR. Such methods can enhance the interpretability of SVR and increase the understanding of the relationships between critical defect features and fatigue life of L-PBF specimens from ML.

PFI measures the importance of a feature by calculating the increase in the model error after permuting the feature. They are illustrated in Figure 5 for the three datasets in this study. As shown in Figure 5, strain amplitude and normalized stress level parameter (adjusted for heat treatment) are dominant features in Dataset 1 since Dataset 1 includes all specimens with different heat treatments and applied strain amplitudes. The results align with our previous correlation analysis in Section 5.2.1. Again, it indicates that due to the inconsistent heat treatment and strain amplitudes, Dataset 1 is not favorable for defect criticality analysis despite its relatively large data size. For Dataset 2 and Dataset 3, while large variations exist in the importance of the defect features, they are not statistically significant. ALE is used to interpret the importance of defect features in Dataset 2 and Dataset 3.

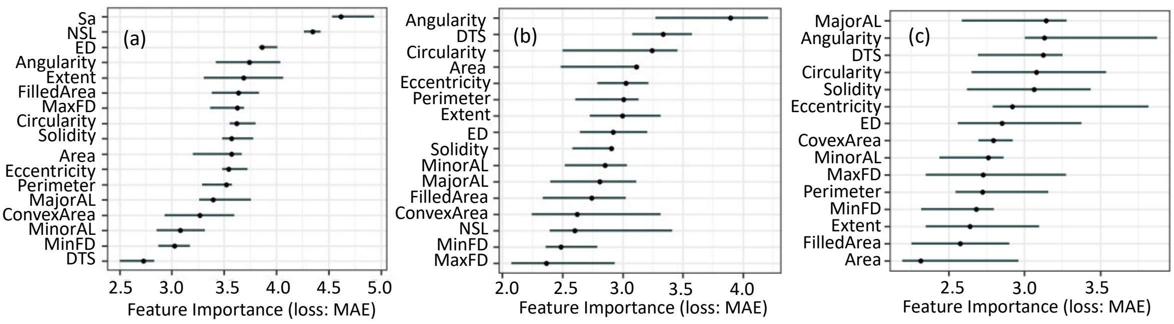

Figure 5. PFI of defect features based on SVR for L-PBF 17-4 PH SS specimens in (a) Dataset 1, (b) Dataset 2, and (c) Dataset 3. (NSL: Normalized stress level; DTS: The distance to the surface; ED: Equivalent diameter; MaxFD: Max Feret diameter; MinFD: Min Feret diameter; MajorAL: Major axis length; MinorAL: Minor axis length)

ALE calculates the marginal effects of the interested features on the fatigue life modeled with SVR by marginalizing other features from its distribution function as in Eq. (6) and Eq. (7) and describes the effects by using the incremental/decremental differences to the fatigue life, indicating as upward/downward trend in ALE plots. ALE plots are used to analyze some important size-related, morphology-related, and location-related defect features identified from PCC, MIC, and PFI above, for Dataset 2 and Dataset 3. Moreover, we further investigate the defects on fractography for explanations of abnormal sections in the general trend on the ALE plots by considering the synergistic effect of the various features on fatigue lives.

(1) <u>ALE plot interpretability and discussion for Dataset 2</u>

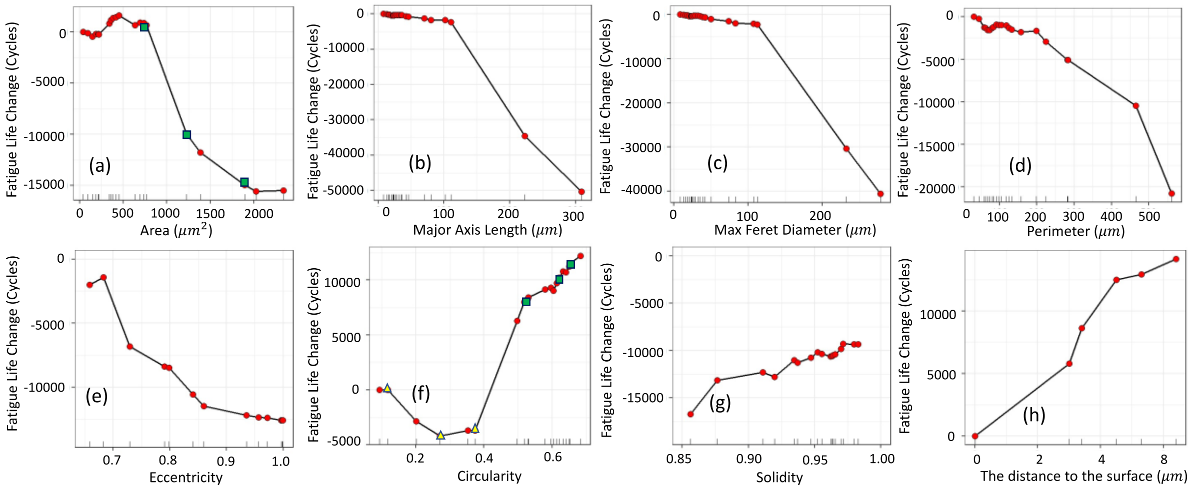

Figure 6. The ALE plots of defect features for SVR, exhibiting their impacts on fatigue life of L-PBF 17-4 PH SS specimens for Dataset 2 (Yellow triangle: abnormal points not on trend; Green rectangle: sampling points on the right trend).

Generally speaking, ALE plots for the eight defect features in Dataset 2 show clear trends regarding fatigue lives due to its relatively large data size, as in Figure 6. It is noted that the increase of all the size-related features (e.g., Area, Major Axis Length, Max Feret Diameter, and perimeter) lead to the decrease of fatigue lives of L-PBF specimens as shown in Figure 6 (a)-(d). For instance, an examination of defects for Area in Figure 6 (a) shows that the defect area only becomes critical after reaching a certain threshold value (around 700–800 μm^2), after which the fatigue lives significantly deteriorate with an increase in size. The defects above the threshold can be classified as large, irregularly shaped LOFs shown in Figure 7 below, while the defects below the threshold could be small gas-entrapped pores. The cracks that grow out of defects larger than 700–800 μm^2 may have already become a long crack, and its growth rate may have been high, which results in shortening the total crack propagation life. Therefore, there is a stronger correlation between life and larger defect sizes. Additionally, in Figure 6 (b)-(d), the general trends show that the fatigue lives decrease with an increase in the values of other size-related features (i.e., major axis length, max Feret diameter, and perimeter).

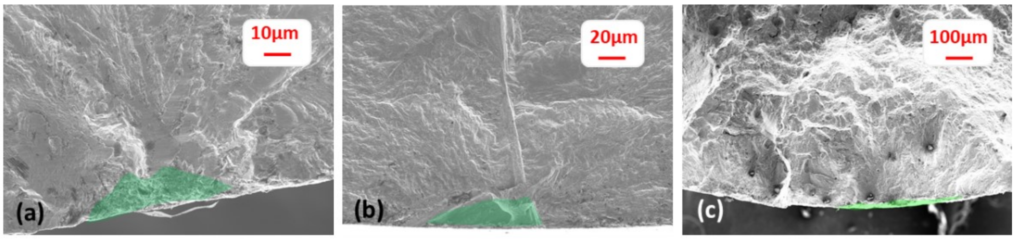

Figure 7. Fatigue crack initiating defects correspond to the three defects with a large area (>700–800 μm^2) and having a large decrease in fatigue lives in Figure 6 (a) marked in green rectangles. They show large size and irregular shapes and could be classified as LOFs.

Furthermore, the general trends of morphology-related defect features (e.g., eccentricity, circularity, solidity) also align with fatigue mechanisms and influencing factors and are verified by PCC in Table 5 as well. For instance, the fatigue lives of specimens tend to be longer if the critical defects are more circular (circularity), have a larger radius of curvature (eccentricity), or/and is more convex with a smoother contour (solidity) if size-related features and distance to the surface are the same. It is noted in Figure 6 (f) that while most defects with circularity (>0.5) show an upward trend that is positively correlated with fatigue lives, several others with small circularity (<0.5) (marked as yellow triangles) have a negative correlation with fatigue lives. We evaluated these defects and found they are irregular (LOFs) and are open to the surface, as shown in Figure 8 (a)-(c) below. Except for these LOFs, it can be seen from Figure 8 (d)-(f), the fatigue lives show an upward trend with the increase of circularity.

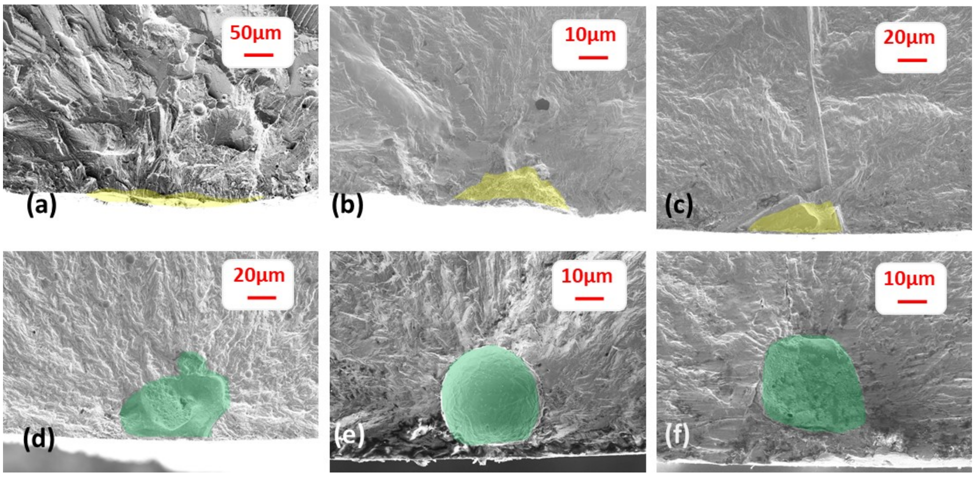

Figure 8. Fatigue crack initiating defects from Dataset 2 for L-PBF 17-4 PH SS specimens with varying circularity values and fatigue lives. As seen in the Fatigue Life vs. circularity ALE plot in Figure 6 (f), the defects with circularity (<0.5) and marked as yellow triangles are defects in (a)-(c), and the defects with circularity (>0.5) and marked as green rectangles are defects in (d)-(f).

Lastly, it is worth noting that the fatigue lives of LB-PBF specimens in Dataset 2 are longer if the critical defects are far away from the surface (i.e., having a large distance to the surface), as shown in Figure 6 (h).

(2) <u>ALE plot interpretability and discussion for Dataset 3</u>

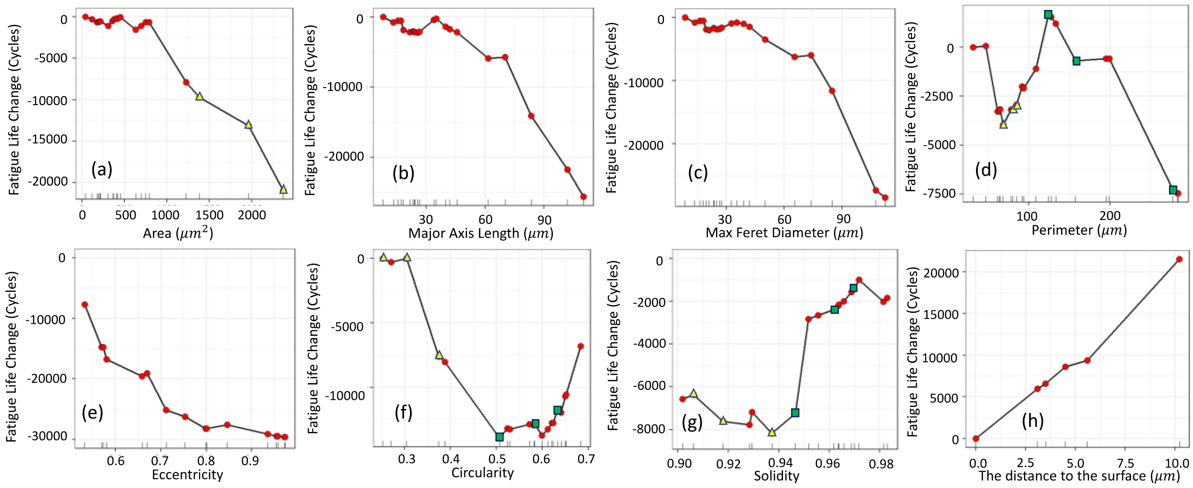

Figure 9. The ALE plots of defect features for SVR, exhibiting their impacts on fatigue life of L-PBF 17-4 PH SS specimens for Dataset 3 (Yellow triangle: abnormal points not on trend; Green rectangle: sampling points on the right trend).

As for Dataset 3, firstly, it is observed that the increase of some size-related features (such as area, major axis length, max Feret diameter) will generally decrease the fatigue lives of L-PBF specimens, as shown a patent downward trend in the above Figure 9 (a)-(c). Such observations align with known fatigue mechanisms and influencing factors and have been reported in Table 5 with negative correlations by PCC. Interestingly, as seen for some of the size-related features, the defect area in Figure 9 (a) only becomes critical after reaching a certain threshold value (around 700–800 μm^2), after which the fatigue lives deteriorate with an increase in size. Inspecting these defects revealed that below this threshold area value, the gas-entrapped pores, which typically are small and circular, are responsible for crack initiation; the defects above the threshold can be classified as large, irregularly shaped LOFs shown in Figure 10 below. The cracks that grow out of defects larger than 700–800 μm^2 may have already become a long crack; its growth rate may have been high, shortening the total crack propagation life. This observation is very similar to Dataset 2 in the previous section. Additionally, in Figure 9 (b) and (c), the general trends show that the fatigue lives decrease with an increase in the values of other size-related features (i.e., major axis length, max Feret diameter).

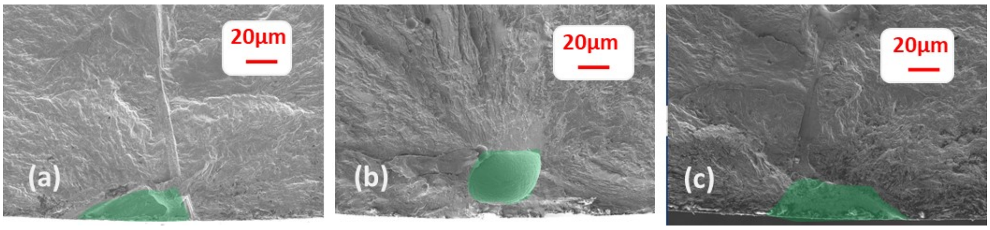

Figure 10. Fatigue crack initiating defects correspond to the three defects with a large area (>700–800 μm^2) and having a large decrease in fatigue lives in Figure 9 (a), marked in green rectangles. They show large size and irregular shapes and could be classified as LOFs.

The relationships between perimeter (also a size-related feature) and fatigue live in Figure 9 (d) do not show a clear trend. As shown in Figure *9* 8 (d), while the defects with a larger perimeter (>100 μm) are on the downward trend of fatigue lives with the increase of perimeter, the defects with a smaller perimeter (<100 μm) have an unusual dip in fatigue lives (a huge decrease and then a rebound in fatigue lives). Three defects at this dip (marked as yellow triangles in Figure 9 (d)) are identified and shown in Figure 11(a)-(c) below. The sharp drop in the fatigue lives with small perimeters could be attributed to their locations (open to the surface), as shown in Figure 11 (a) and (b). When the defects with a small perimeter move away from the surface, as shown in Figure 11 (c), the fatigue lives rebound. Moreover, three defects after the dip on the downward trend are sampled, marked as green rectangles in Figure 9 (d), and shown in Figure 11 (d)-(f) here. Their increasing perimeters can correlate with the decreasing trend of fatigue lives. Additionally, as shown in Figure 11 (f), the defect with the largest perimeter (~300 μm) and open to the surface has a substantial decrease in the fatigue life.

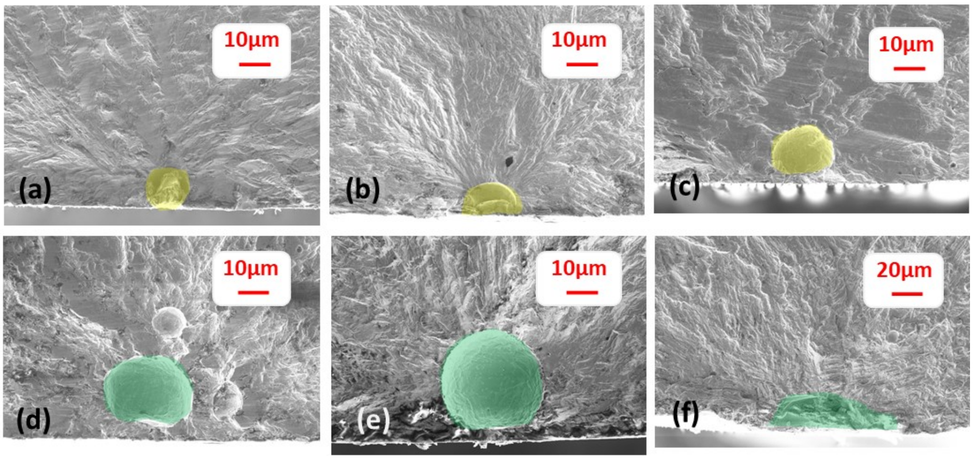

Figure 11. Fatigue crack initiating defects from Dataset 3 for L-PBF 17-4 PH SS specimens with varying perimeter values and fatigue lives. As seen in the Fatigue Life vs. Perimeter ALE plot in Figure 9 (d), the defects with a small perimeter (<100 µm) and marked as yellow triangles are defects in (a)-(c), and the defects with a large perimeter (>100 µm) and marked as green rectangles are defects in (d)-(f).

Secondly, it is noticed in Figure 9 (e) that as the eccentricity value increases, the fatigue lives decrease, since a large eccentricity means the defect has a long major axis length and it is noncircular. This feature is strongly correlated with major axis length and the maximum Feret diameter (as seen in **Error! Reference source not found.**), which is also reflected in the similar trends observed for these size-related features. Similarly, for defects with high values of circularity and solidity, fatigue lives are higher. This is due to the defects having smoother contours, a larger radius of curvature, and a smaller size often, which is accompanied by a reduction in the local stress concentrations, and thus, leading to better fatigue lives. We further examine the impact of circularity and solidity on fatigue life in the following two paragraphs since there are some abnormal sections in the general trend on the ALE plots with Dataset 3 in Figure 9 (f)-(g).

PCC in Table 5 suggests that the fatigue lives of specimens with large circularity values tend to be long. Defects with high circularity (>0.5) in Figure 9 (f) do show an upward trend with positive correlations with fatigue lives. However, a few defects with small circularity (<0.5) (marked as yellow triangles in Figure 9 (f)) indicate abnormal negative correlations. We identify these defects and present them in Figure 12 (a)-(c) below. These defects are irregular (LOFs) and are open to the surface, which will have largely decreased fatigue lives; especially for the defect in Figure 12 (c), it has a large area of 1382.667 µm^2. After the dip, it can be seen from Figure 12 (d)-(f), the fatigue lives are on the upward trend with the increase of circularity.

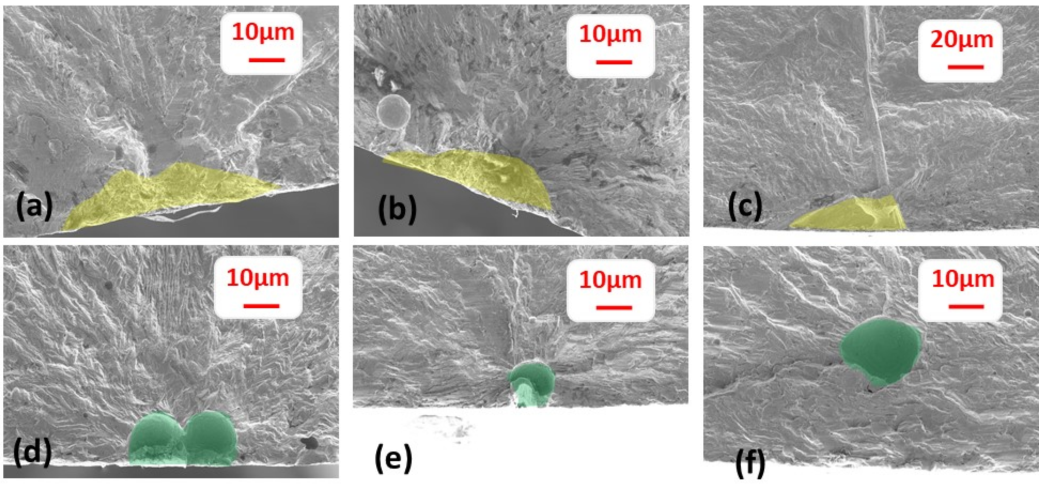

Figure 12. Fatigue crack initiating defects from Dataset 3 for L-PBF 17-4 PH SS specimens with varying circularity values and fatigue lives. As seen in the Fatigue Life vs. circularity ALE plot in Figure 9 (f), the defects with circularity (<0.5) and marked as yellow triangles are defects in (a)-(c), and the defects with circularity (>0.5) and marked as green rectangles are defects in (d)-(f).

PCC in Table 5 also suggests the fatigue lives of specimens with large solidity values tend to be long because a large solidity indicates the defect is close to a convex shape and might have a smooth boundary and be gas-entrapped pores. This aligns with the upward trend in Figure 9 (g) except for a few defects with solidity less than 0.94 having an excessive reduction in fatigue lives. These defects (marked as yellow triangles in Figure 9 (g)) are shown in Figure 13 (a)-(c), and it is noticed that they are open to the surface and their areas are large, relative to defects (marked as green rectangles in Figure 9 (g)) in Figure 13 (d)-(f).

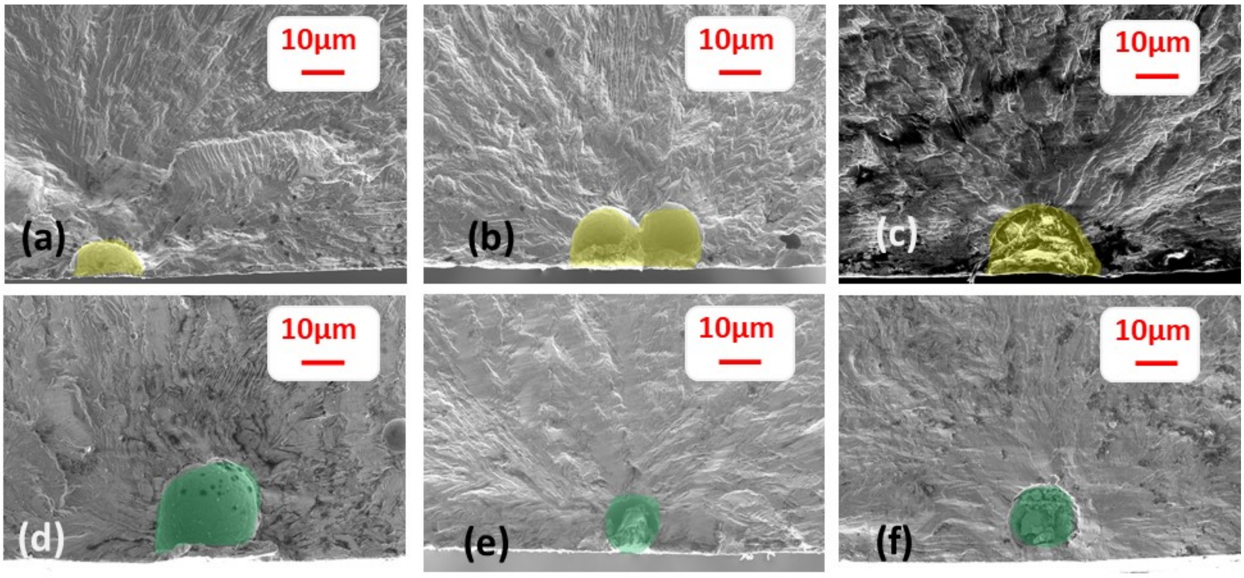

Figure 13. Fatigue crack initiating defects from Dataset 3 for L-PBF 17-4 PH SS specimens with varying solidity values and fatigue lives. As seen in the Fatigue Life vs. solidity ALE plot in Figure 9 (g), the defects with solidity

(<0.94) and marked as yellow triangles are defects in (a)-(c), and the defects with circularity (>0.94) and marked as green rectangles are defects in (d)-(f).

Finally, Figure 9 (h) shows that defects with a shorter distance to the surface lead to shorter fatigue lives of L-PBF specimens. This can be attributed to the presence of higher stress concentrations when defects are close to the surface, as has also been seen through FE modeling in literature where the highest stress concentrations were found for defects less than one diameter away from the free surface [58].

In summary, ALE plots provide a promising analytical way to explore and interpret the correlations between defect features and fatigue lives of L-PBF specimens. In practice, especially when data are limited, combining both size and morphology-related features and considering the synergistic effect of the various features on fatigue lives can give better interpretations.

6. Conclusions and Future Work

In this study, we developed an IDADC for L-PBF fatigue performance assessment from critical defect features. It is a novel integration of domain expertise and data-driven methods for potential qualification of L-PBF components. The proposed IDADC incorporates defect feature extraction from fractography images of L-PBF fatigue test specimens, correlation analysis, and defect-fatigue relationships modeling with ML to achieve an accurate and interpretable data-driven fatigue analysis. Specifically, based on SEM images acquired from the fracture surfaces of L-PBF 17-4 PH SS specimens tested under strain-controlled, fully reversed fatigue loading, CBIR is applied to extract various size-related and morphology-related defect features from the critical defects. Then, correlation analysis and SVR are employed to understand the relationships between these defect features and the fatigue life of the specimens. The analysis reveals the correlations between critical defect features and the fatigue life, which align with the known fatigue mechanisms and influencing factors. To summarize the findings of this study:

- Defect size, distance to the surface, circularity, and smooth contours were found to have strong relationships with the fatigue life of L-PBF specimens. SVR achieved relatively accurate fatigue life modeling based on defect features, especially with the specimens which had undergone the same heat treatment and were tested under the same strain amplitude (MAPE = 0.101).

- PFI and ALE were incorporated to interpret the relationships from SVR outcomes, revealing morphology-related features (such as eccentricity, circularity, and solidity) and size-related features (such as maximum ferret diameter, perimeter, and area) have a significant impact on the fatigue life of L-PBF specimens. They provided useful interpretable insights from "black-box" ML models.

The IDADC has the potential practical benefits to nondestructive inspections with 3D X-ray CT scans in the future, which become the mainstream in describing defects in L-PBF specimens [14, 16-18, 59] and studying L-PBF fatigue properties:

(1) To identify the critical defects in L-PBF specimens from 3D X-ray CT scans: X-ray CT scans can capture the size-related, morphology-related, and distance-related defect features for all the defects in the scanned areas. The IDADC and the insights from this study can be easily extended to the nondestructive defect inspection and identify the critical defects that may initiate cracks in the parts during cyclic service loading. Such an understanding will potentially enable a nondestructive qualification of additively manufactured parts for fatigue-critical applications by utilizing an X-ray CT and scanning the critical locations of the parts that experience higher stress.

(2) To understand the most critical defect features of the different types of defects (i.e., LOFs and keyholes) in AM materials in 3D, correlate them to the L-PBF process parameters, and study their impacts on the fatigue behavior of AM materials. The insights obtained can be used to optimize process parameters to avoid such defect types and/or reduce the intensity of such features, therefore improving the fatigue lives of the AM materials.

(3) To reinforce the fidelity of defect features with strong correlations: Some features are more sensitive to X-ray CT inspection resolutions (e.g., circularity) than others (e.g., volume, major axis length). The strong correlations among these features can be used to adjust the measurements to a reasonable accuracy. For instance, circularity and major axis length have a strong correlation (~0.7), as shown in PCC analysis in Section 5.2.2. Since circularity is

difficult to capture with low-resolution X-ray CT, we can leverage its strong correlation with major axis length, which is still accurately measured with low inspection resolution, to adjust the measurement to a statistically more accurate circularity value. This benefit is particularly useful for 3D scanning for a large part with a limited resolution.

The authors' forthcoming research will focus on the three future aspects of this work: (1) develop a comprehensive defect characterization framework for L-PBF parts on 2D fractography images by leveraging particle morphological analysis techniques in geology and biology, and advanced techniques in statistics and image/signal processing; (2) extend defect characterization to 3D X-ray CT scans to identify critical defect features and enable nondestructive fatigue performance analysis from 3D X-ray CT scans; and (3) leverage deep learning to ensure high model accuracy to examine the effects of defects and microstructure, as well as their interactions, on fatigue performance of L-PBF parts.

Declaration of Competing Interest

The authors declare that they have no known competing financial interests or personal relationships that could have appeared to influence the work reported in this paper.

Acknowledgments

This material is based upon work partially funded by the National Science Foundation (NSF) under award No. 2134689 and the National Institute of Standards and Technology (NIST) under award No. 70NANB19H170.

Disclaimer

Nima Shamsaei is the Guest Editor of the International Journal of Fatigue (IJF) Special Issue (SI) on Additive Manufacturing (AM). The editorial and peer-review process for this article was handled by the journal's Editors-in-Chief. Furthermore, the authors of this article do not have access to any confidential information related to its peer-review process.

Reference

[1] S. K. Everton, M. Hirsch, P. Stravroulakis, R. K. Leach, and A. T. Clare, "Review of in-situ process monitoring and in-situ metrology for metal additive manufacturing," *Materials Design,* vol. 95, pp. 431-445, 2016.

[2] P. K. Rao, J. P. Liu, D. Roberson, Z. J. Kong, and C. Williams, "Online real-time quality monitoring in additive manufacturing processes using heterogeneous sensors," *Journal of manufacturing science and engineering,* vol. 137, no. 6, 2015.

[3] S. Ford and M. Despeisse, "Additive manufacturing and sustainability: an exploratory study of the advantages and challenges," *Journal of Cleaner Production,* vol. 137, pp. 1573-1587, 2016.

[4] N. Guo and M. C. Leu, "Additive manufacturing: technology, applications and research needs," *Frontiers of Mechanical Engineering,* vol. 8, no. 3, pp. 215-243, 2013.

[5] N. Shamsaei, A. Yadollahi, L. Bian, and S. M. Thompson, "An overview of Direct Laser Deposition for additive manufacturing; Part II: Mechanical behavior, process parameter optimization and control," *Additive Manufacturing,* vol. 8, pp. 12-35, 2015.

[6] R. DeVor, S. Kapoor, J. Cao, and K. Ehmann, "Transforming the landscape of manufacturing: distributed manufacturing based on desktop manufacturing (DM) 2," *Journal of manufacturing science and engineering,* vol. 134, no. 4, 2012.

[7] A. Ghobadian, I. Talavera, A. Bhattacharya, V. Kumar, J. A. Garza-Reyes, and N. O'regan, "Examining legitimatisation of additive manufacturing in the interplay between innovation, lean manufacturing and sustainability," *International Journal of Production Economics,* vol. 219, pp. 457-468, 2020.

[8] "Additive Manufacturing Market by Technology " AMPOWER Report, , 2020. [Online]. Available: https://additive-manufacturing-report.com/additive-manufacturing-market/

[9] A. Yadollahi and N. Shamsaei, "Additive manufacturing of fatigue resistant materials: Challenges and opportunities," *International Journal of Fatigue,* vol. 98, pp. 14-31, 2017.

[10] S. Romano, A. Brückner-Foit, A. Brandão, J. Gumpinger, T. Ghidini, and S. Beretta, "Fatigue properties of AlSi10Mg obtained by additive manufacturing: Defect-based modelling and prediction of fatigue strength," *Engineering Fracture Mechanics,* vol. 187, pp. 165-189 2018.

[11] R. Cunningham, S. P. Narra, C. Montgomery, J. Beuth, and A. D. Rollett, "Synchrotron-based X-ray microtomography characterization of the effect of processing variables on porosity formation in laser power-bed additive manufacturing of Ti-6Al-4V," *JOM,* vol. 69, no. 3, pp. 479-484, 2017.

[12] A. J. Sterling, B. Torries, N. Shamsaei, S. M. Thompson, and D. W. Seely, "Fatigue behavior and failure mechanisms of direct laser deposited Ti–6Al–4V," *Materials Science and Engineering: A,* vol. 655, pp. 100-112, 2016.

[13] M. Seifi *et al.*, "Progress towards metal additive manufacturing standardization to support qualification and certification," *JOM,* vol. 69, no. 3, pp. 439-455, 2017.

[14] A. du Plessis, I. Yadroitsava, and I. Yadroitsev, "Effects of defects on mechanical properties in metal additive manufacturing: A review focusing on X-ray tomography insights," *Materials & Design,* vol. 187, pp. 108385-108385, 2020, doi: https://doi.org/10.1016/j.matdes.2019.108385.

[15] M. Tang and P. C. Pistorius, "Fatigue life prediction for AlSi10Mg components produced by selective laser melting," *International Journal of Fatigue,* vol. 125, pp. 479-490, 2019, doi: https://doi.org/10.1016/j.ijfatigue.2019.04.015.

[16] N. Sanaei, A. Fatemi, and N. Phan, "Defect characteristics and analysis of their variability in metal L-PBF additive manufacturing," *Materials & Design,* vol. 182, pp. 108091-108091, 2019, doi: https://doi.org/10.1016/j.matdes.2019.108091.

[17] S. Tammas-Williams, P. J. Withers, I. Todd, and P. B. Prangnell, "The Influence of Porosity on Fatigue Crack Initiation in Additively Manufactured Titanium Components," *Scientific Reports,* vol. 7, no. 1, pp. 7308-7308, 2017, doi: 10.1038/s41598-017-06504-5.

[18] I. Maskery *et al.*, "Quantification and characterisation of porosity in selectively laser melted Al–Si10–Mg using X-ray computed tomography," *Materials Characterization,* vol. 111, pp. 193-204, 2016, doi: https://doi.org/10.1016/j.matchar.2015.12.001.

[19] R. Shrestha, N. Shamsaei, M. Seifi, and N. Phan, "An investigation into specimen property to part performance relationships for laser beam powder bed fusion additive manufacturing," *Additive Manufacturing,* vol. 29, p. 100807, 2019.

[20] A. Fatemi *et al.*, "Fatigue behaviour of additive manufactured materials: An overview of some recent experimental studies on Ti-6Al-4V considering various processing and loading direction effects," *Fatigue & Fracture of Engineering Materials & Structures,* vol. 42, no. 5, pp. 991-1009, 2019.

[21] R. Molaei *et al.*, "Fatigue of additive manufactured Ti-6Al-4V, Part II: The relationship between microstructure, material cyclic properties, and component performance," *International Journal of Fatigue,* vol. 132, p. 105363, 2020.

[22] J. W. Pegues *et al.*, "Fatigue of additive manufactured Ti-6Al-4V, Part I: The effects of powder feedstock, manufacturing, and post-process conditions on the resulting microstructure and defects," *International Journal of Fatigue,* vol. 132, p. 105358 2020.

[23] C. M. Bishop, *Pattern recognition and machine learning*. springer, 2006.

[24] R. I. Stephens, A. Fatemi, R. R. Stephens, and H. O. Fuchs, *Metal fatigue in engineering*. John Wiley & Sons, 2000.

[25] J. Tavernelli and L. Coffin Jr, "Experimental support for generalized equation predicting low cycle fatigue," 1962.

[26] R. Wei, "Fracture mechanics approach to fatigue analysis in design," 1978.

[27] S. Bhat and R. Patibandla, "Metal fatigue and basic theoretical models: a review," *Alloy Steel-Properties and Use,* vol. 22, 2011.

[28] U. Zerbst, M. Madia, C. Klinger, D. Bettge, and Y. Murakami, "Defects as a root cause of fatigue failure of metallic components. I: Basic aspects," *Engineering Failure Analysis,* vol. 97, pp. 777-792, 2019.

[29] H. Kitagawa, "Applicability of fracture mechanics to very small cracks or the cracks in the early stage," *Proc. of 2nd ICM, Cleveland, 1976,* pp. 627-631, 1976.

[30] Y. Murakami, *Metal fatigue: effects of small defects and nonmetallic inclusions*. Academic Press, 2019.

[31] Y. Murakami and S. Beretta, "Small defects and inhomogeneities in fatigue strength: experiments, models and statistical implications," *Extremes,* vol. 2, no. 2, pp. 123-147, 1999.

[32] F. Stern, J. Tenkamp, and F. Walther, "Non-destructive characterization of process-induced defects and their effect on the fatigue behavior of austenitic steel 316L made by laser-powder bed fusion," *Progress in Additive Manufacturing,* vol. 5, no. 3, pp. 287-294, 2020.

[33] S. Romano, A. Brandão, J. Gumpinger, M. Gschweitl, and S. Beretta, "Qualification of AM parts: Extreme value statistics applied to tomographic measurements," *Materials & Design,* vol. 131, pp. 32-48, 2017.

[34] Y. Hu *et al.*, "A new approach to correlate the defect population with the fatigue life of selective laser melted Ti-6Al-4V alloy," *International Journal of Fatigue,* vol. 136, p. 105584, 2020.

[35] J.-R. Poulin, A. Kreitcberg, P. Terriault, and V. Brailovski, "Fatigue strength prediction of laser powder bed fusion processed Inconel 625 specimens with intentionally-seeded porosity: Feasibility study," *International Journal of Fatigue,* vol. 132, p. 105394, 2020.

[36] B. Torries, A. Imandoust, S. Beretta, S. Shao, and N. Shamsaei, "Overview on microstructure-and defect-sensitive fatigue modeling of additively manufactured materials," *Jom,* vol. 70, no. 9, pp. 1853-1862, 2018.

[37] D. Kotzem *et al.*, "Impact of single structural voids on fatigue properties of AISI 316L manufactured by laser powder bed fusion," *International Journal of Fatigue,* vol. 148, p. 106207, 2021.

[38] D.-F. Li, R. A. Barrett, P. E. O'Donoghue, N. P. O'Dowd, and S. B. Leen, "A multi-scale crystal plasticity model for cyclic plasticity and low-cycle fatigue in a precipitate-strengthened steel at elevated temperature," *Journal of the Mechanics and Physics of Solids,* vol. 101, pp. 44-62, 2017.

[39] B. Smith, D. Shih, and D. McDowell, "Cyclic plasticity experiments and polycrystal plasticity modeling of three distinct Ti alloy microstructures," *International Journal of Plasticity,* vol. 101, pp. 1-23, 2018.

[40] D. L. McDowell, "Multiscale crystalline plasticity for materials design," in *Computational Materials System Design*: Springer, 2018, pp. 105-146.

[41] G. M. Castelluccio and D. L. McDowell, "A mesoscale approach for growth of 3D microstructurally small fatigue cracks in polycrystals," *International Journal of Damage Mechanics,* vol. 23, no. 6, pp. 791-818, 2014.

[42] V. Prithivirajan, P. Ravi, D. Naragani, and M. D. Sangid, "Direct comparison of microstructure-sensitive fatigue crack initiation via crystal plasticity simulations and in situ high-energy X-ray experiments," *Materials & Design,* vol. 197, p. 109216, 2021.

[43] A. Fatemi and D. F. Socie, "A critical plane approach to multiaxial fatigue damage including out-of-phase loading," *Fatigue & Fracture of Engineering Materials & Structures,* vol. 11, no. 3, pp. 149-165, 1988.

[44] C. Wang, X. Tan, S. Tor, and C. Lim, "Machine learning in additive manufacturing: State-of-the-art and perspectives," *Additive Manufacturing,* p. 101538, 2020.

[45] M. Yang, K. Kpalma, and J. Ronsin, "A Survey of Shape Feature Extraction Techniques," P.-Y. Yin Ed.: IN-TECH, 2008, pp. 43-90.

[46] P. D. Nezhadfar *et al.*, "Fatigue crack growth behavior of additively manufactured 17-4 PH stainless steel: Effects of build orientation and microstructure," *International Journal of Fatigue,* vol. 123, pp. 168-179, 2019.

[47] P. D. Nezhadfar, R. Shrestha, N. Phan, and N. Shamsaei, "Fatigue behavior of additively manufactured 17-4 PH stainless steel: Synergistic effects of surface roughness and heat treatment," *International Journal of Fatigue,* vol. 124, pp. 188-204, 2019.

[48] N. Altman and M. Krzywinski, "Association, correlation and causation," ed: Nature Publishing Group, 2015.

[49] D. N. Reshef *et al.*, "Detecting novel associations in large data sets," *science,* vol. 334, no. 6062, pp. 1518-1524, 2011. [Online]. Available: https://www.ncbi.nlm.nih.gov/pmc/articles/PMC3325791/pdf/nihms358982.pdf.

[50] H. Drucker, C. J. Burges, L. Kaufman, A. J. Smola, and V. Vapnik, "Support vector regression machines," in *Advances in neural information processing systems*, 1997, pp. 155-161.

[51] M. Awad and R. Khanna, "Support Vector Regression," in *Efficient Learning Machines: Theories, Concepts, and Applications for Engineers and System Designers*. Berkeley, CA: Apress, 2015, pp. 67-80.

[52] A. J. Smola and B. Schölkopf, "A tutorial on support vector regression," *Statistics and Computing,* vol. 14, no. 3, pp. 199-222, 2004/08/01 2004, doi: 10.1023/B:STCO.0000035301.49549.88.

[53] M. T. Ribeiro, S. Singh, and C. Guestrin, "Model-agnostic interpretability of machine learning," *arXiv preprint arXiv:1606.05386,* 2016.

[54] P. D. Nezhadfar, R. Shrestha, N. Phan, and N. Shamsaei, "Fatigue data for laser beam powder bed fused 17-4 PH stainless steel specimens in different heat treatment and surface roughness conditions," *Data in brief,* vol. 25, p. 104215, 2019.

[55] A. Soltani-Tehrani, J. Pegues, and N. Shamsaei, "Fatigue behavior of additively manufactured 17-4 PH stainless steel: The effects of part location and powder re-use," *Additive Manufacturing,* vol. 36, p. 101398, 2020.

[56] P. Nezhadfar, R. Shrestha, N. Phan, and N. Shamsaei, "Fatigue data for laser beam powder bed fused 17-4 PH stainless steel specimens in different heat treatment and surface roughness conditions," *Data in brief,* vol. 25, p. 104215, 2019.

[57] *ASTM A693-16 Standard Specification for Precipitation-Hardening Stainless and Heat-Resisting Steel Plate, Sheet, and Strip*, A. International, West Conshohocken, PA, 2016. [Online]. Available: www.astm.org

[58] Z. Xu, W. Wen, and T. Zhai, "Effects of pore position in depth on stress/strain concentration and fatigue crack initiation," *Metallurgical and Materials Transactions A,* vol. 43, no. 8, pp. 2763-2770, 2012.

[59] J. Liu, C. Liu, Y. Bai, P. Rao, C. B. Williams, and Z. Kong, "Layer-wise spatial modeling of porosity in additive manufacturing," *IISE Transactions,* vol. 51, no. 2, pp. 109-123, 2019/02/01 2019, doi: 10.1080/24725854.2018.1478169.